

1

2

Geophysical Research Letters

3

Supporting Information for

4

**P-wave Reflectivity of the Crust and Upper Mantle Beneath the Southern
Appalachians and Atlantic Coastal Plain using Global Phases**

5

6

7

Devon N. Verellen¹, Erik C. Alberts², Gustavo A. Larramendi, E. Horry Parker, Jr.³, and Robert
B. Hawman

8

9

Department of Geology, University of Georgia, Athens, GA, USA

10

11

¹now at Chevron, Houston TX

12

²now at Exxon/Mobil, Houston, TX

13

³now at Black & Veatch, Greenville, SC

14

15

16

17

Contents of this file

18

19

Text S1

20

Figures S1 to S11

21

Table S1

22

23

Introduction

24

We show the distribution (Figure S1) and summarize the parameters (Table S1) of earthquakes
used in this study and present additional stacked sections for Lines D, E, and W (Figures S2-S5).

25

26

We then discuss measures of vertical and lateral resolution and investigate the generation of
artifacts associated with source-side scattering and differential moveout of PKPdf and PKiKP
arrivals (Figures S6-S9). Finally, we describe a simple algorithm for migrating data recorded
with unevenly spaced stations and show preliminary results (Figures S10-S11).

27

28

29

30

31

32

33

34 **Text S1.**

35

36 **1. Additional Stacked Sections**

37

38 Here we present a map showing the distribution of earthquakes used in this study (Figure S1) and
39 additional stacked sections showing Moho reflections beneath Line D (Figure S2) and Line E
40 (Figure S3) and stacked sections plotted with both normal and reverse polarity to more clearly
41 show reflections from the upper mantle beneath Line E (Figure S4) and Line W (Figure S5).

42

43 **2. Resolution**

44

45 Dominant periods in the deconvolved sections range from 1-4 seconds. Quarter-wavelength
46 estimates of vertical resolution range from 1–1.5 km in the crust ($V_p = 3.5\text{-}6.5$ km/s) to 3-8 km in
47 the upper mantle ($V_p = 8.1$ km/s). Corresponding estimates of lateral resolving power, as
48 measured by the radius of the first Fresnel zone for incident plane waves, range from 3–16 km
49 within the crust to 20-65 km at depths of 70-250 km within the mantle. Lateral resolving power
50 will also depend on station spacings, which vary from 3.5-42 km along the W line, 4.5–43 km
51 along the E line, and 5–29 km along the D line. For future work, projections of TA stations
52 (Figure 1) onto the SESAME lines will be used to fill in some of the gaps in coverage [*Hopper et*
53 *al.*, 2016].

54

55 **3. Processing Artifacts: Comparison of Deconvolution, Autocorrelation, and** 56 **Crosscorrelation for Long-Duration Effective Source Wavelets**

57

58 Effective source wavelets for the shallower-focus earthquakes used in this study include
59 significant energy associated with underside reflections, e.g., pPKPdf and sPKPdf, in the source
60 region. Here we examine the ability of deconvolution to recover reflections at later two-way
61 times where portions of the effective source wavelets extend beyond the listening window. To
62 examine this issue, we use the estimates of source wavelets derived by stacking waveforms for
63 stations deployed north of the Coastal Plain, as described in the main text, for all the earthquakes
64 listed in Table S1. We construct synthetic seismograms by convolving these estimates with a
65 series of 6 impulses representing the direct PKPdf arrival and a pseudo-random time distribution
66 of 5 reflections, then add low-level ($S/N \sim 10$) random noise. Reflections are assigned a uniform
67 amplitude, equal to half that of the direct arrival. We then deconvolve each seismogram using the
68 input source wavelet and a range of Gaussian smoothing parameters ($\alpha = 1.0 - 4.0$).

69

70 The results for most of the earthquakes show clear pulses at the expected travel times for the four
71 earliest reflections, along with various levels of noise between reflections and before the direct
72 arrival. As expected, for later reflections where the effective source wavelets extend beyond the
73 listening window, reflection amplitudes are not fully recovered (Figures S6c – S6g). This can
74 also generate spurious energy in the later portions of the traces (e.g., Figure S6c). Stacking the
75 traces, using the same combinations of earthquakes used to generate the stacks of real data in
76 Figures 2-4 and S2-S5, suppresses these artifacts (Figure S7).

77

78 Autocorrelation of the same input traces also recovers reflections but with higher levels of noise;
79 in this case, the noise is more evenly distributed over the length of each trace. As expected, cross
80 correlation of the input trace with the effective source wavelet is more successful than
81 autocorrelation in recovering reflection amplitudes, but sidelobes remain a problem because of
82 narrower bandwidths compared with the deconvolved traces. This is particularly evident for
83 events 9 and 7 (Figures S6e and S6f). Again, stacking helps to suppress this noise (Figure S7).

84
85
86
87
88
89
90
91
92
93
94
95
96
97
98
99
100
101
102
103
104
105
106
107
108
109
110
111
112
113
114
115
116
117
118
119
120
121
122
123
124
125
126
127
128
129
130
131
132
133
134

As noted in the text, the estimation of effective source wavelets can be complicated by the arrival of two phases (PKPdf and PKiKP) in the time window of interest. For a source depth of 100 km and distances of 115°-140°, travel times for the two phases differ by ~ 0-3 s and ray parameters differ by 0.01–0.26 s/°. For the earthquakes used in this study, the effective array apertures for stations deployed north of the Coastal Plain ranged from 1.7°–2.6° and the differential moveouts ranged from 0.1-0.4 s. The stacking procedure described in the text treats all these phases (including source-side scattering) as a single arrival and therefore yields an effective source wavelet of extended duration, with some loss of resolution at higher frequencies. Differential moveouts for PKPdf and PKiKP between those stations and the southernmost stations range from 0.1-1.1 s; this causes some broadening of deconvolved waveforms (Figure S8) that is minimized by stacking (Figure S9).

4. Migration

4.1. Migration Method

As noted in the main text, stacking of waveforms for multiple earthquakes may degrade rather than enhance some signals. To preserve signal levels and to construct a more complete image of reflectivity, we migrate events observed for individual earthquakes and then stack the results to form composite cross sections. However, as noted in the above discussion of processing artifacts, care must be exercised before incorporating coherent energy observed in the later portions of the sections.

After deconvolving waveforms for a given earthquake, we divide the traces along each line (D, E, and W) into shorter-aperture gathers (to allow for local variations in travel times and apparent dips of reflections) and slant stack to obtain objective measures of apparent slowness and coherence of reflected arrivals. Reflections are assumed to arrive as plane waves across each subset of stations. Coherence is measured using semblance [Neidell and Taner, 1971]. Following Stoffa *et al.* [1981], we then apply a coherency filter derived from the smoothed semblance to suppress noise. Alternative measures of coherence such as signal polarity [Hansen *et al.*, 1988] can also be used. The choice of coherency thresholds is based on the levels required to fully suppress noise preceding the direct arrival.

Standard migration algorithms require input traces that are evenly spaced. Because this requirement is violated by the SESAME array, we are experimenting with alternative methods. For the examples shown in Figures S10 and S11, we use a modification of an approach developed for sparse wide-angle reflection data [Hawman, 2008]. This somewhat rudimentary algorithm is based on a simple line drawing but retains some characteristics of the original wavefield. In common with methods developed by Phinney and Jurdy [1979] and Milkereit [1987], it uses the slant stack as an intermediate data set. As implemented here, apparent horizontal slownesses are measured relative to the zero slowness value assigned to the aligned first arrival (PKPdf). The algorithm treats each sample in the coherency-filtered slant stack as a reflection from an interface at depth. Each reflection is assumed to arrive as a plane wave across the input subsection. The algorithm proceeds by downward continuing each sample through an assumed velocity model along a ray defined by the appropriate positive or negative horizontal slowness. A reflector segment then is constructed with a dip determined by the horizontal slowness and layer velocity and a width controlled by the subsection aperture and Fresnel radius. The process then is repeated for neighboring (or overlapping) subsections to build a subsurface image. The edges of individual reflector segments sometimes show concave upward curvature. These “smiles” are measures of the degree of smearing of individual peaks in the slant stack and thus serve as useful

135 measures of the resolving power of the component subsections [Hawman, 2008] and scatter in
136 travel times due to statics variations.

137

138 Migration velocity models are constructed for different stations along the SESAME array using a
139 combination of COCORP images of Triassic rift basin and Coastal Plain sediments [McBride et
140 al., 1989; Barnes and Reston, 1992] and previous wide-angle [Hawman et al., 2012] and SsPmp
141 [Parker et al., 2016] analyses of the study area for the crystalline crust. For the preliminary
142 images shown here, we used a constant value of 8.1 km/s for the velocity of the upper mantle. As
143 expected for the nearly vertical incidence angles for PKPdf/PKiKP, most of the coherent energy
144 in the slant stacks is concentrated at very small apparent slownesses (-0.05 to +0.05 s/km),
145 corresponding to small apparent dips. The partial migrated images from individual trace
146 subsections then are summed to construct a composite migrated section (Figures S10 and S11).

147

148 Gaps in subsurface coverage due to inactive stations are gradually filled in by stacking results for
149 multiple earthquakes. For stations deployed in the Coastal Plain, we are also experimenting with
150 predictive deconvolution [Robinson and Treitel, 1980; Yu et al., 2015] to suppress multiples
151 generated within Cretaceous and younger sediments and underlying Triassic/Jurassic extensional
152 basins.

153

154 **4.2. Preliminary Migration Results**

155

156 Preliminary migrated images (Figures S10 and S11) are based on vertical stacks for 7-8
157 earthquakes, with no contributions from TA stations, and therefore are rather sparse. They will
158 certainly change as more events are added. Although the migration velocity models incorporate
159 layers representing low-velocity sediments of the Coastal Plain and underlying rift basins, no
160 attempt has been made to remove the effects of multiples generated within those sequences. At
161 the risk of reading too much into the results at this early stage of analysis, we note the following:

162

163 **1)** The section for Line W across the Atlantic coastal plain shows concentrations of reflections at
164 depths of 50-75 km (just below Moho), 90-110 km, 140-160 km, 180-200 km, and 250-270 km
165 (Figure S10).

166

167 **2)** The section for Line D, trending NW across the Carolina Terrane, Inner Piedmont, and Blue
168 Ridge shows a similar clustering of reflections at depths greater than 90 km, but the zone of
169 highly reflectivity at 50-75 km is absent (Figure S11). One possible interpretation is that the 50-
170 75 km zone beneath the Coastal Plain represents layers within the upper mantle depleted by
171 partial melting during Mesozoic extension and underplating of the crust [Pollitz and Mooney,
172 2016]. The absence of this zone beneath Line D (Figure S11) would be consistent with more
173 limited extension of inboard terranes, as suggested by the lack of Triassic dikes northwest of the
174 Inner Piedmont [King, 1961]. More detailed tracking of this zone, in particular, using wide-angle
175 reflections to constrain lower crustal velocities (e.g., Marzen et al., 2019) could be used to help
176 establish the northwest extent of major alteration of the crust and uppermost mantle associated
177 with the breakup of Pangaea.

178

179 **3)** Overall, the sections over the Carolina Terrane, Inner Piedmont, and Blue Ridge (Line D and
180 northern half of Line W) show a concentration of reflectors at depths of roughly 140-160 km,
181 consistent with shearing just below the LAB and in agreement with recent tomography results
182 that show a roughly 150-km thick lithosphere beneath the Grenville province and Appalachian
183 Mountains [Savage et al., 2017].

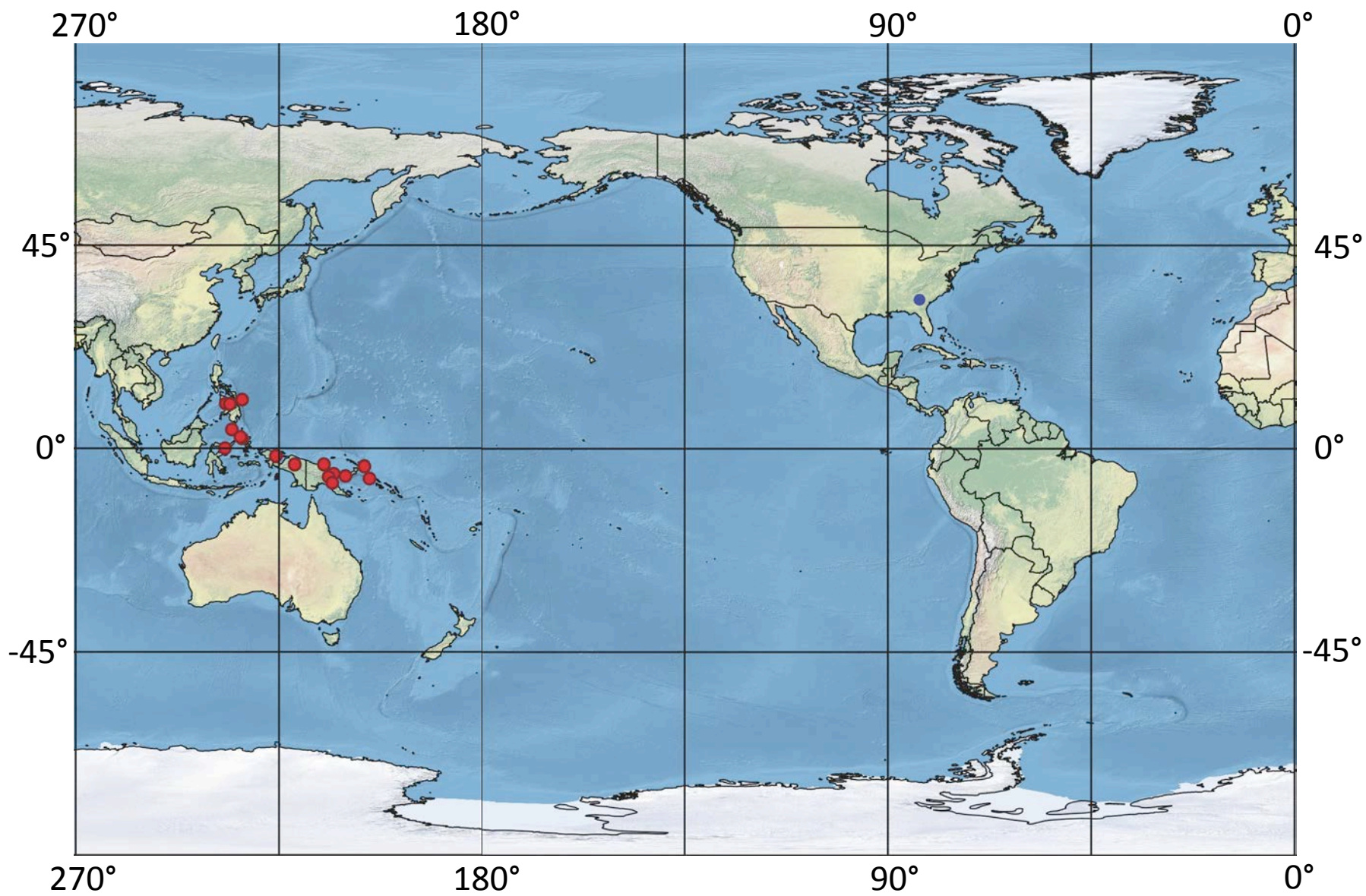


Figure S1

Figure S1. Locations of 16 earthquakes (red circles) used for the analysis of PKPdf - generated reflections. Blue circle indicates the average location of SESAME stations.

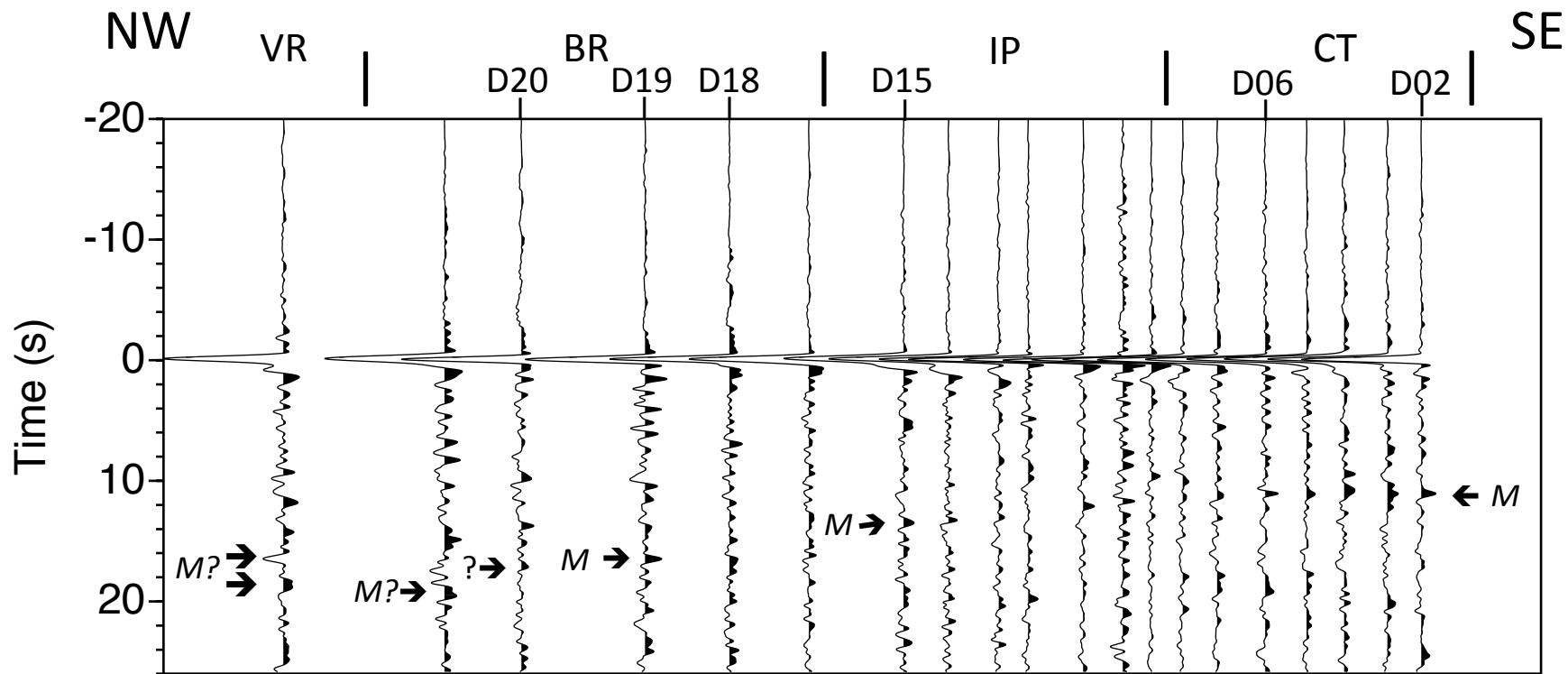


Figure S2

Figure S2. Stacks of deconvolved records ($\alpha=4.0$) for 16 earthquakes (Table S1) showing PKPdf-generated reflections beneath SESAME Line D. Stations D01 and D16 were never deployed. Prior to stacking, traces were normalized by the RMS value for the 18-s noise window preceding the direct PKPdf arrival to give greater weight to seismograms with higher signal levels. Samples have been multiplied by a factor equal to the square root of two-way time to smoothly increase amplitudes for later reflections. The arrival at 0 s is the deconvolved waveform for PKPdf. Upon reflection at the free surface, this arrival reverses polarity. Therefore, reflections from positive impedance contrasts (lower velocity over higher velocity) will have a polarity opposite to the polarity of PKPdf.

The stack is plotted with reverse polarity (negative polarity for the direct PKPdf arrival). M: pulse interpreted as the reflection from the Moho. This increases in travel time from 11.2 s (crustal thickness: 36.4 km, assuming an average P-wave velocity of 6.5 km/s) at station D02 (Carolina Terrane) northward to 13.5 s (43.9 km) at station D15 (Inner Piedmont). These times are consistent (to within 0.1 – 0.3 s) with arrivals interpreted as Moho reflections in coincident, reprocessed COCORP lines [Cook and Vesudevan, 2006]. Those authors were not able to identify Moho north of station D18, but the stacked section shows strong arrivals interpreted as Moho reflections at station D19 (16.5 s) and D20 (17.2 s) in the Blue Ridge Mountains. Corresponding crustal thicknesses, again assuming an average P-wave velocity of 6.5 km/s, are 54 and 56 km. This increase mimics the trend observed for Line W (Figure 2). These estimates are also consistent with values obtained from Ps receiver functions that suggest a similar increase in crustal thickness from 36.2 km at station D02 to 57 km at station D20 [Parker *et al.*, 2013; 2015]. They are also consistent with earlier estimates derived from wide-angle data [Hawman *et al.*, 2012], suggesting that the southern Appalachian highlands are in rough isostatic equilibrium.

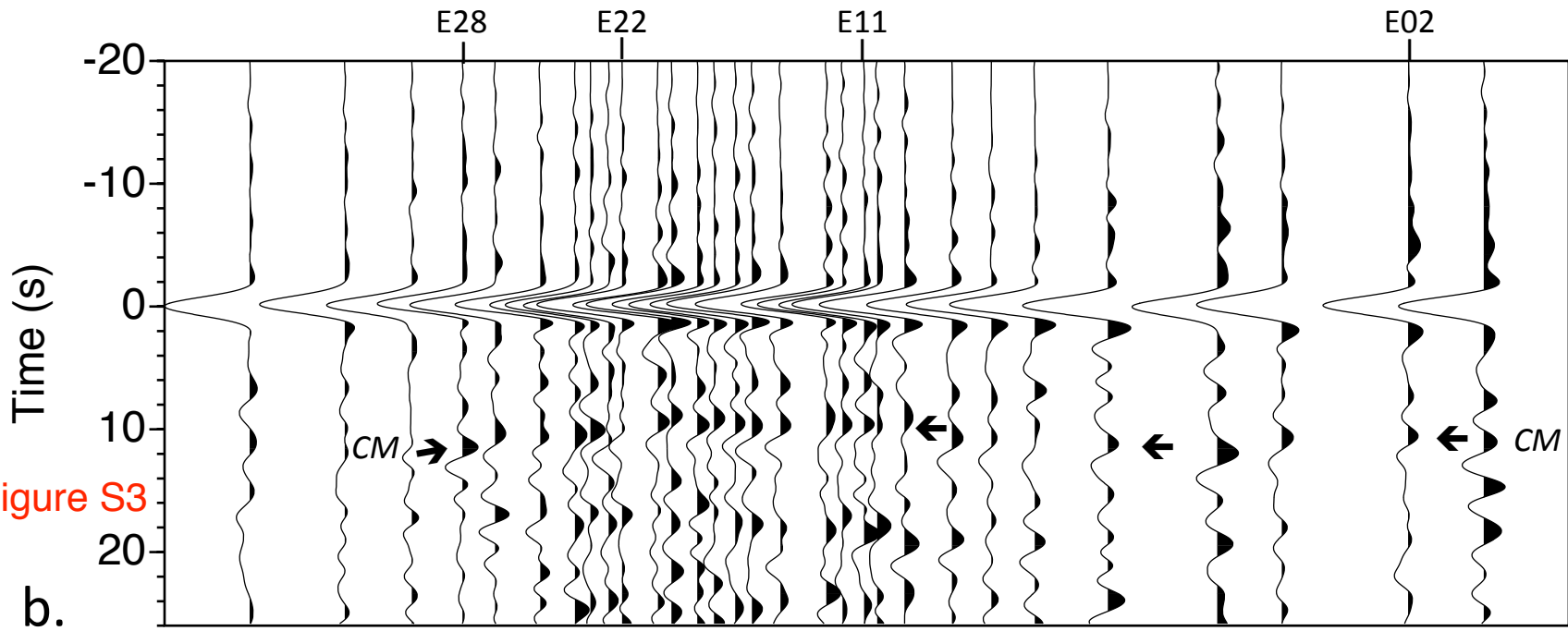
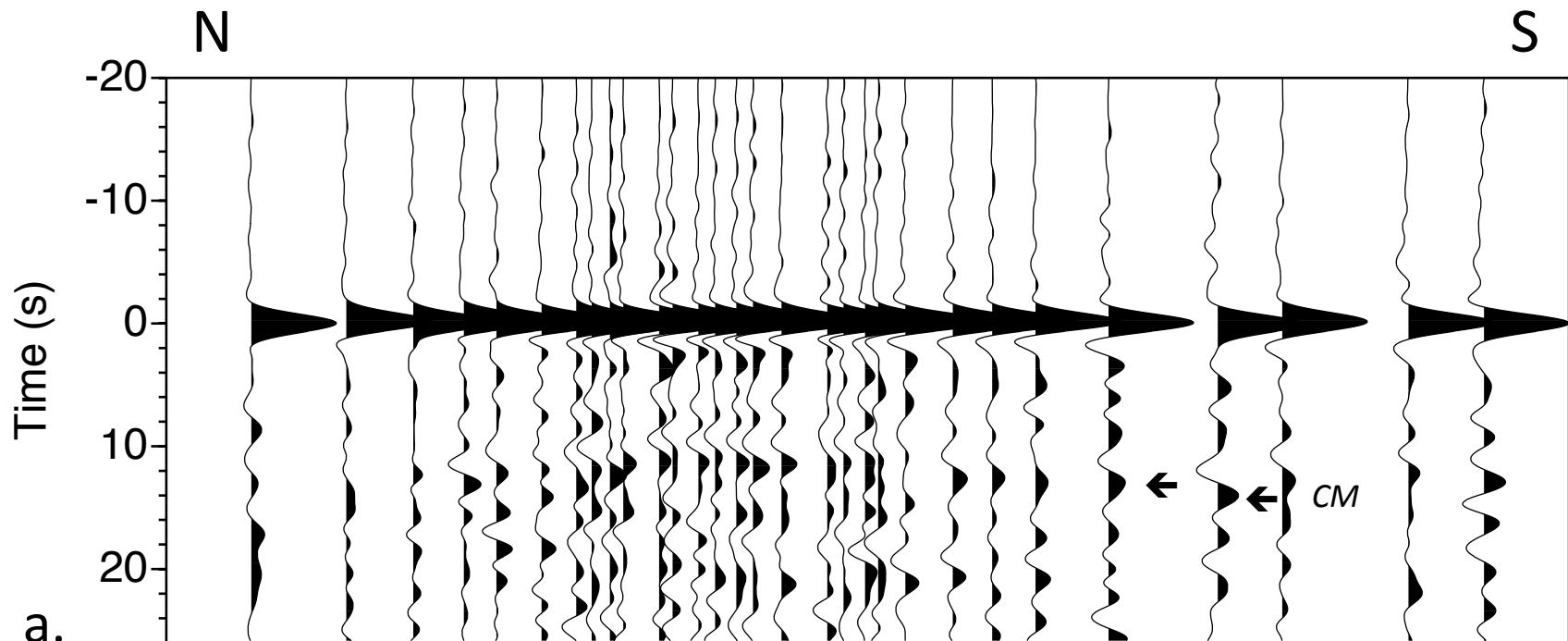


Figure S3

Figure S3. Stacks of deconvolved records ($\alpha=1.0$) for 8 earthquakes (Table S1) for SESAME Line E (deployed a year after Lines W and D). Station E14 was never deployed. The stack is plotted with both normal and reverse polarity to more clearly show the reflections.

- a)** Stack plotted with normal polarity (positive polarity for the direct PKPdf arrival).
- b)** Stack plotted with reverse polarity (negative polarity for PKPdf).

Assuming a simple first-order discontinuity, the Moho would be expected to generate a positive polarity reflection on the reverse polarity sections. Travel times for this pulse are 10.4 – 10.6 s for stations E02 and E03, then decrease to a minimum of 8.9 – 9.9 s for stations E11 – E22. Moho times along coincident COCORP stations [*McBride, 1991*] are greater, between (10.5 – 11.3 s); as suggested for Line W, the disparity may be due in part to the broader depth range of reflectors sampled by the broader PKPdf-generated waveforms. From E23 to E28, Moho times increase from 10.1 – 11.4 s, in better agreement with the COCORP times (10.5 – 11.6 s). The Moho times observed in this study agree to within 0.1 – 1.7 s with normal-incidence times predicted for models derived from SsPmp arrivals [*Parker et al., 2016*]. Taken together, the multicyclic reflections “CM” at roughly 9-12 s on the normal and reverse polarity sections are interpreted as a layered crust-mantle transition at depths of approximately 30-37 km.

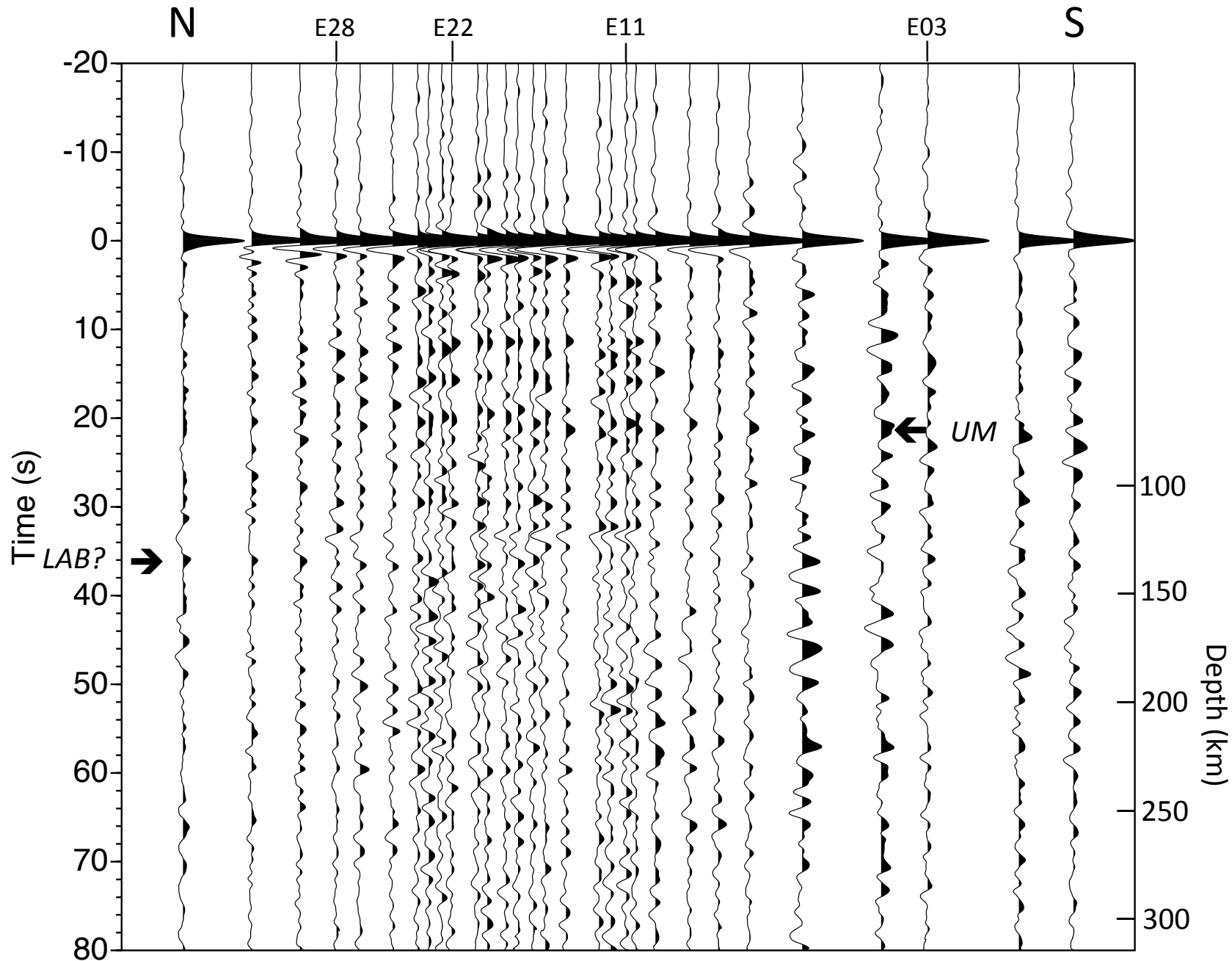


Figure 4

a.

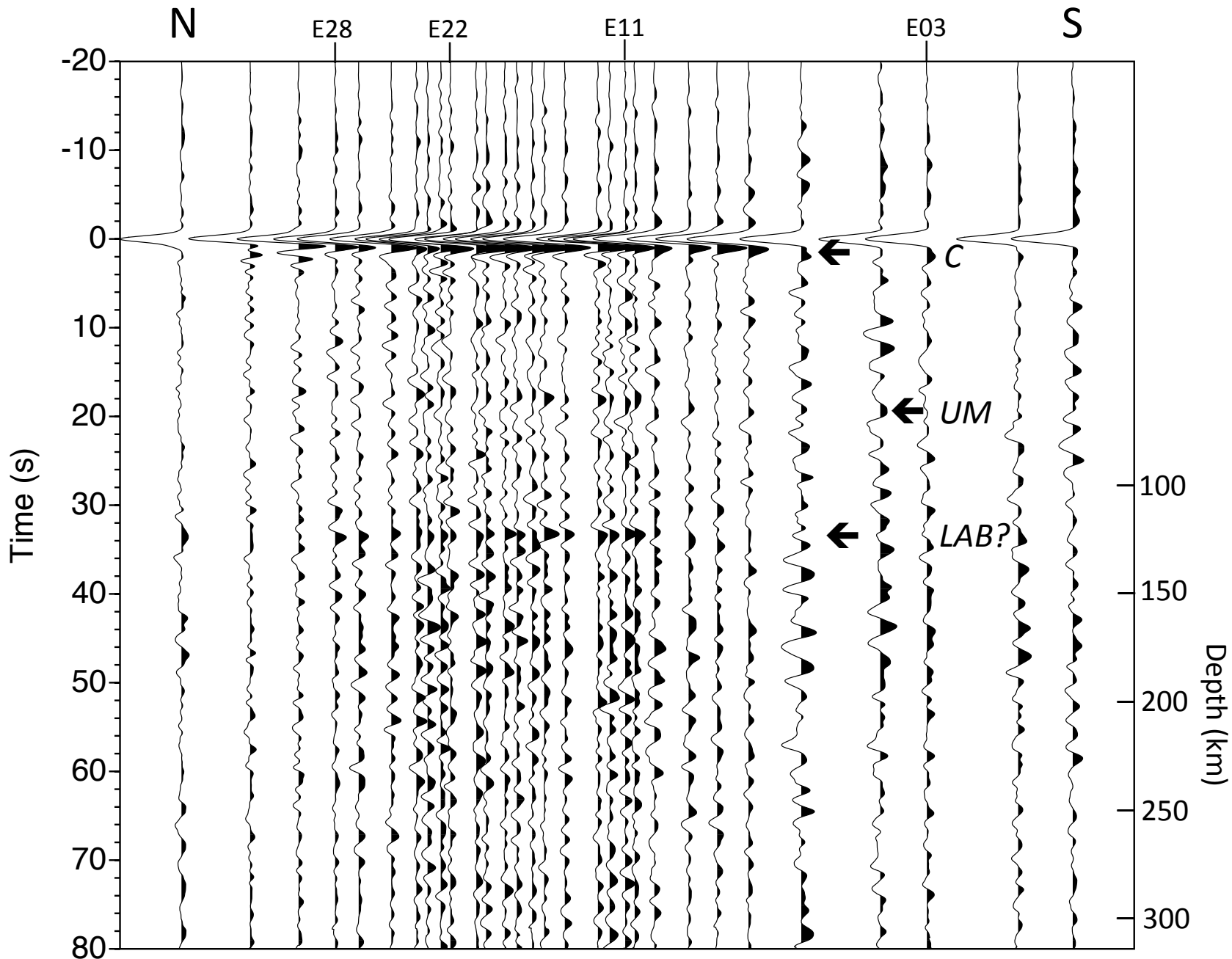
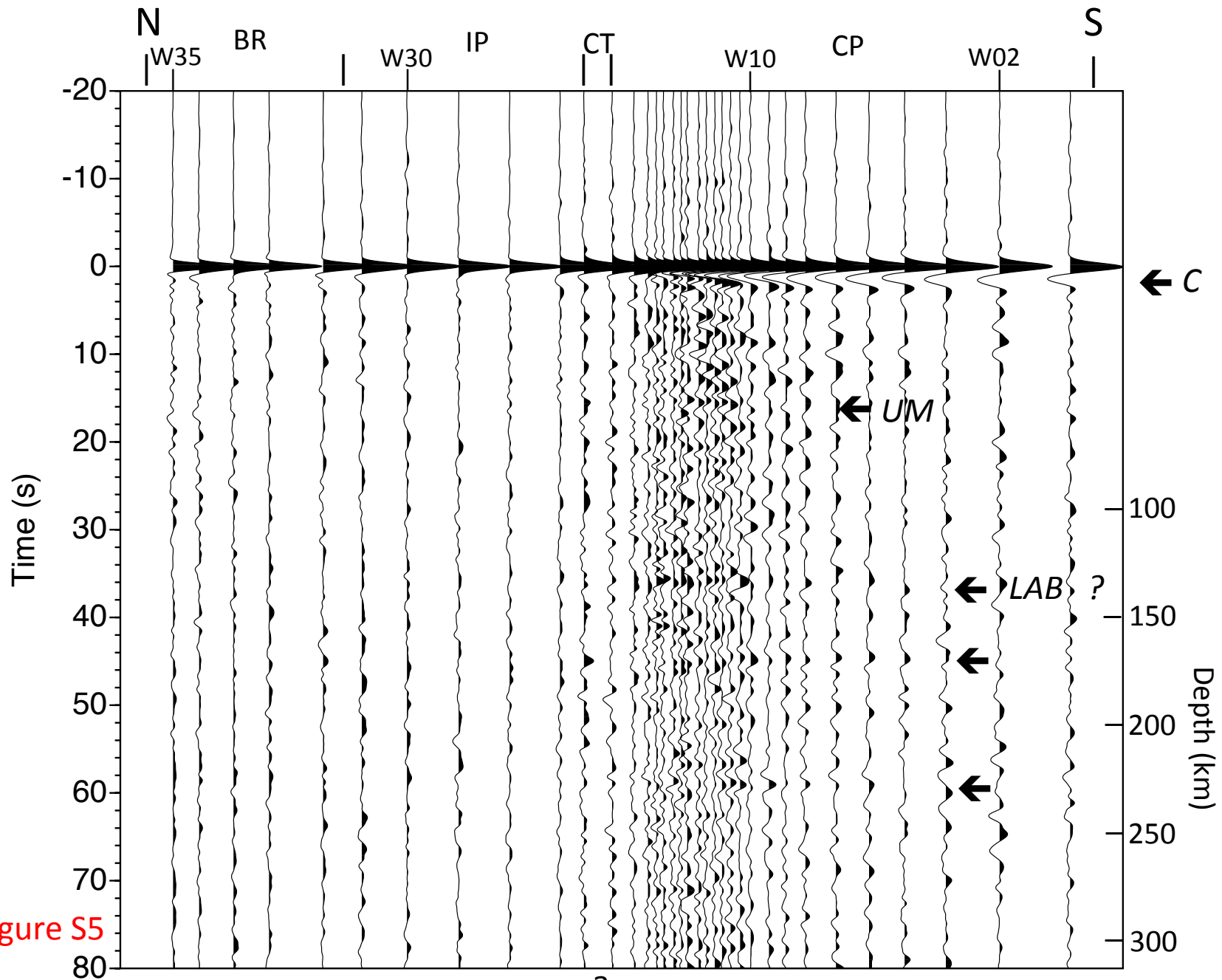


Figure S4

b.

Figure S4. Stacks of deconvolved records ($\alpha=2.0$) for 6 earthquakes (Table S1) showing PKPdf-generated reflections from the crust and uppermost mantle beneath SESAME Line E. Station E14 was never deployed. Plotted with both normal and reverse polarity to more clearly show the reflections. Depths are approximated using a laterally uniform velocity model with a crustal thickness of 55 km and average velocities of 6.5 km/s for the crust and 8.1 km/s for the upper mantle. This approximation contributes 0.5-2.5 km to uncertainties in depth within the mantle. (a) Plotted with normal polarity. (b) Plotted with reverse polarity (same as Figure 3). C: interpreted as the reflection from the base of Cretaceous-Tertiary sediments and poorly consolidated sedimentary rocks. Times are consistent with well data. Reflections from the crust-mantle transition are more clearly shown in Figure S3. UM: reflections arriving between 16 and 20 s, possibly generated by layers within the uppermost mantle depleted by partial melting during Mesozoic extension [*Pollitz and Mooney, 2016*]. Multicyclic reflections observed at 34–36 s (~127-135 km) may mark the effects of shearing in the vicinity of the LAB and/or intrusions triggered by partial melting of hydrated asthenosphere.



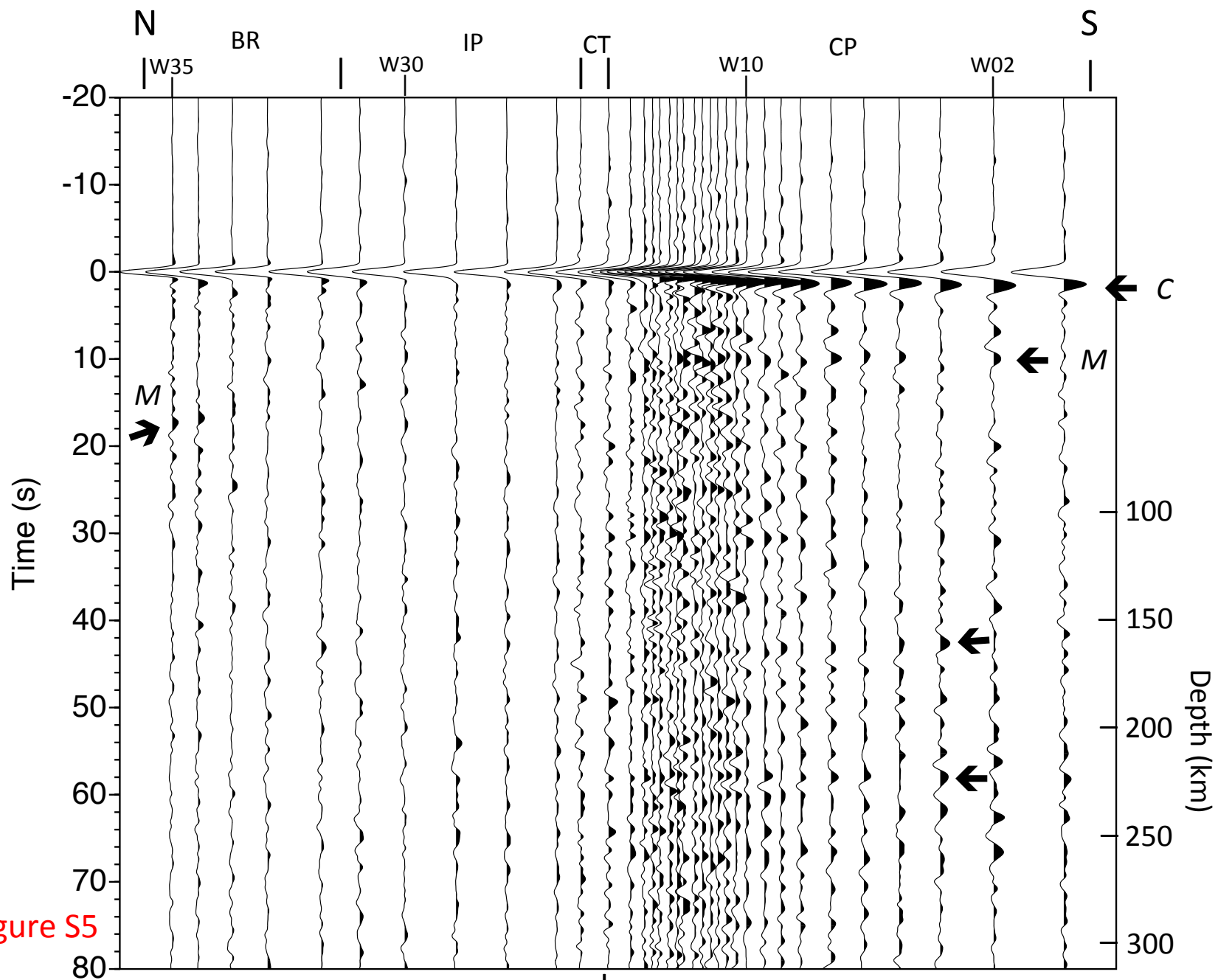


Figure S5

b.

Figure S5. Stacks of deconvolved records ($\alpha=2.0$) for 16 earthquakes (Table S1) showing PKPdf-generated reflections from the crust and upper mantle beneath SESAME Line W, plotted with both normal and reverse polarity to more clearly show the waveforms. Station W25 was never deployed. (a) plotted with normal polarity (same as Figure 4). UM: reflection from the uppermost mantle, less continuous than the event observed beneath Line E (Figure S4). C: reflection from the base of Cretaceous and Tertiary sediments and poorly consolidated sedimentary rocks (see also Figure 2). This arrival shallows towards the north and projects to the surface near the observed feather edge of Coastal Plain sediments. (b) plotted with reverse polarity. M: arrival interpreted as the reflection from the Moho (see also Figure 2). The arrival at 35 s (depth approximately 130 km) is in close agreement with arrivals interpreted as the LAB in Figure S4b. Later arrivals (arrows) at roughly 44 s and 58 s (~167 km and 224 km) are interpreted as reflections from layering within the asthenosphere.

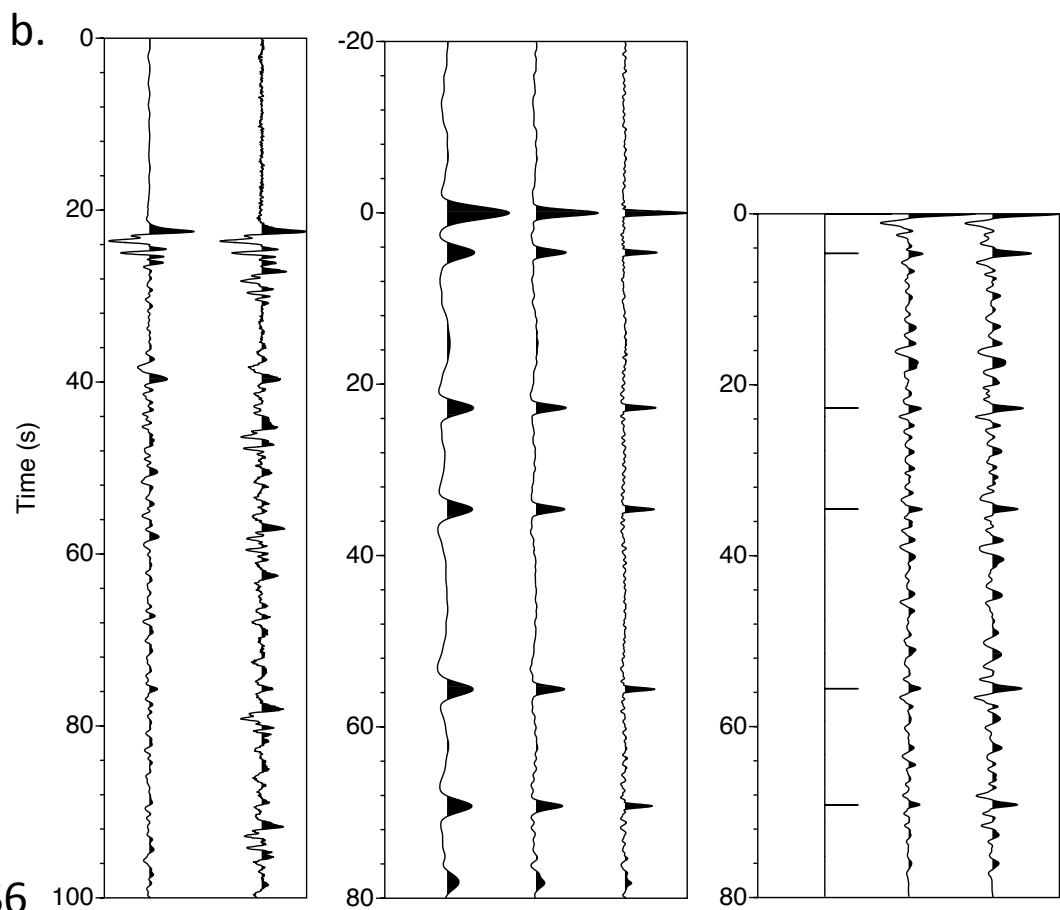
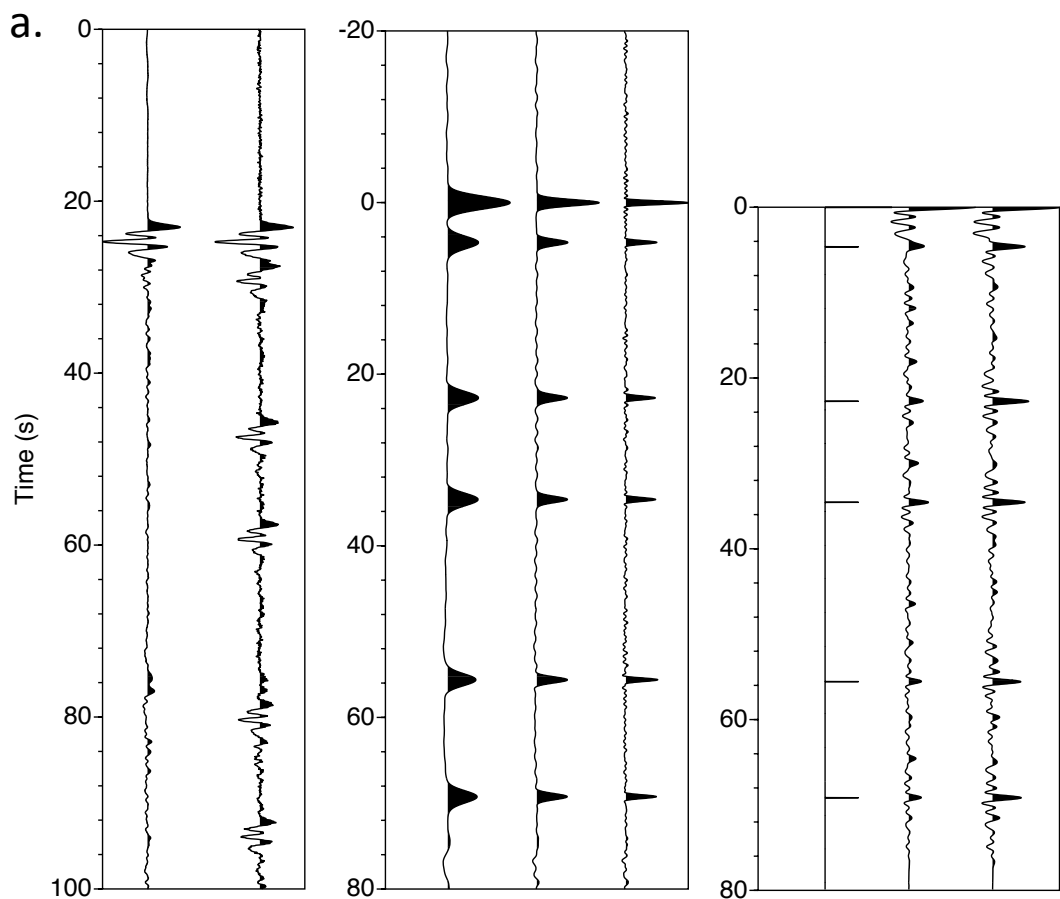


Figure S6

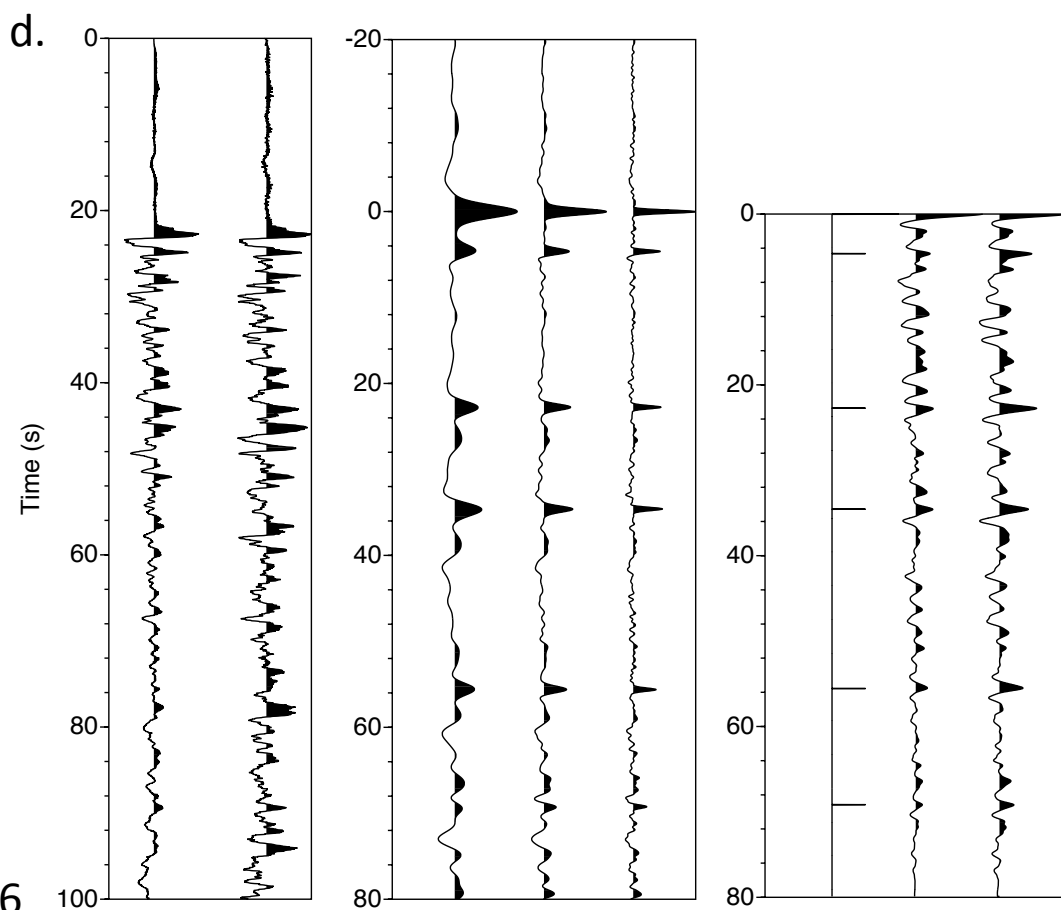
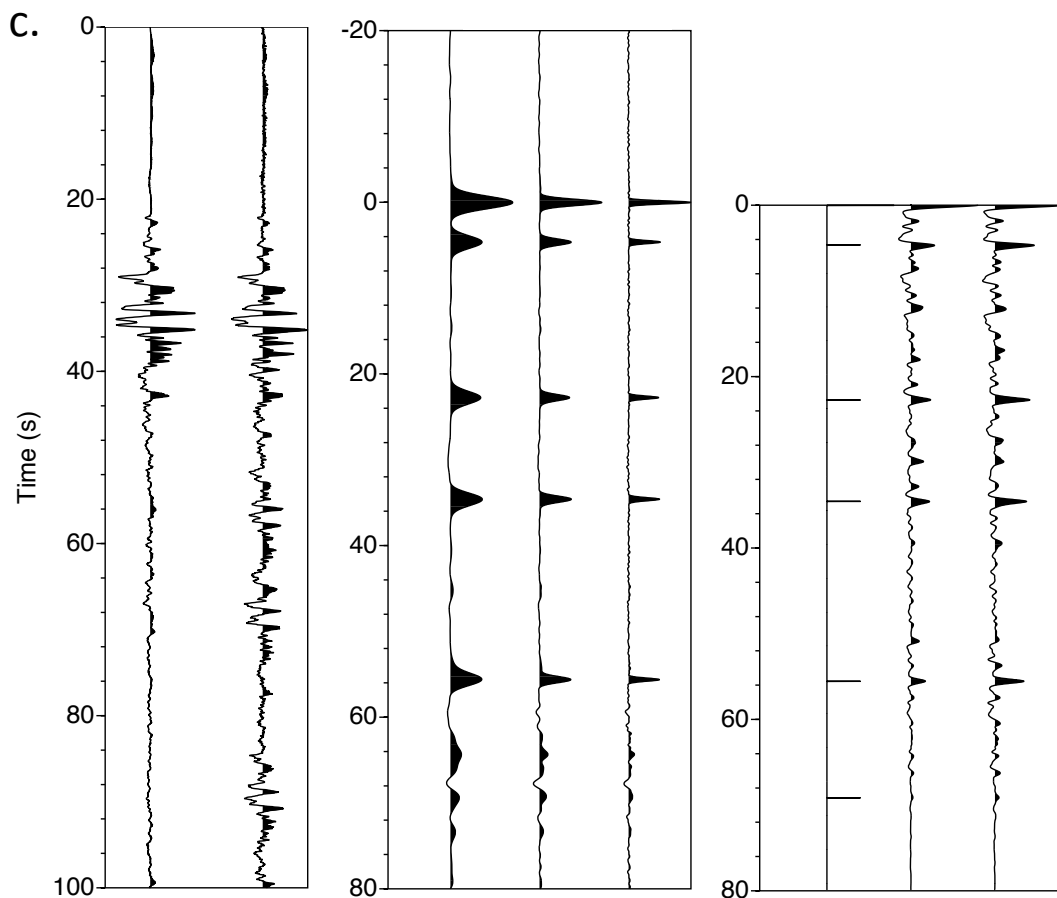


Figure S6

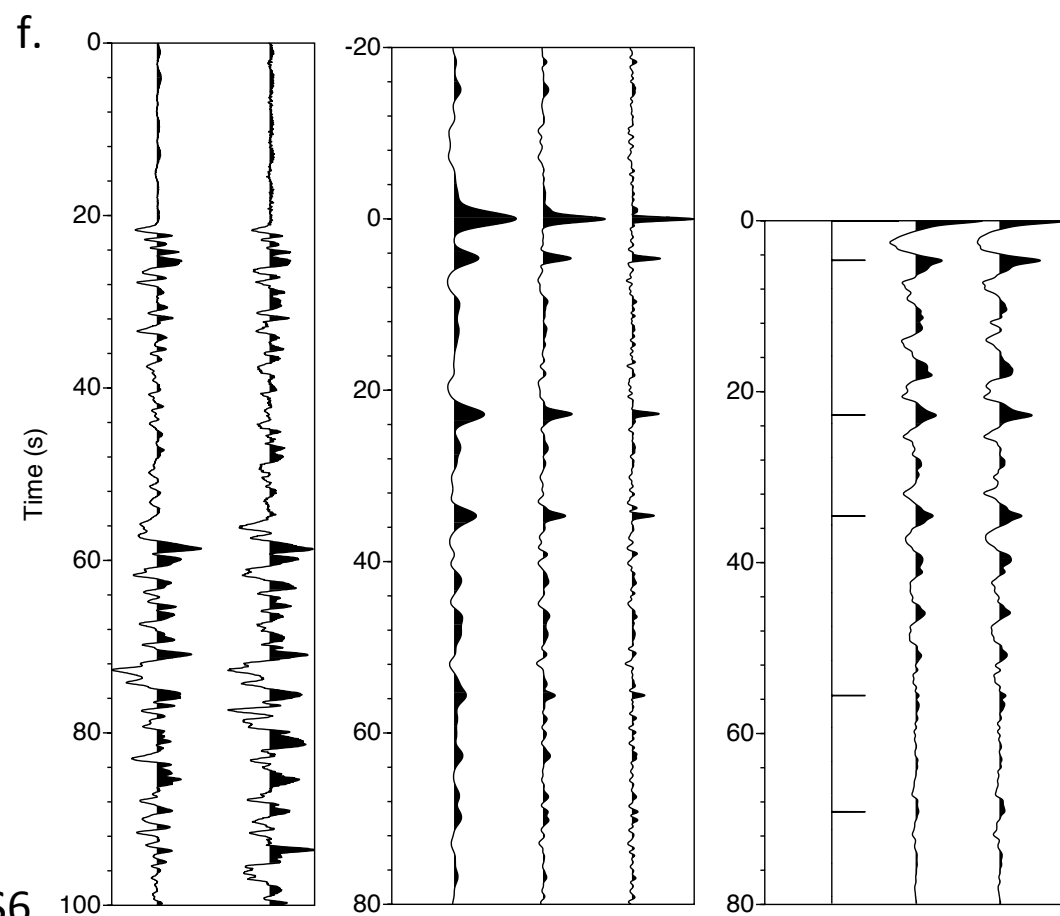
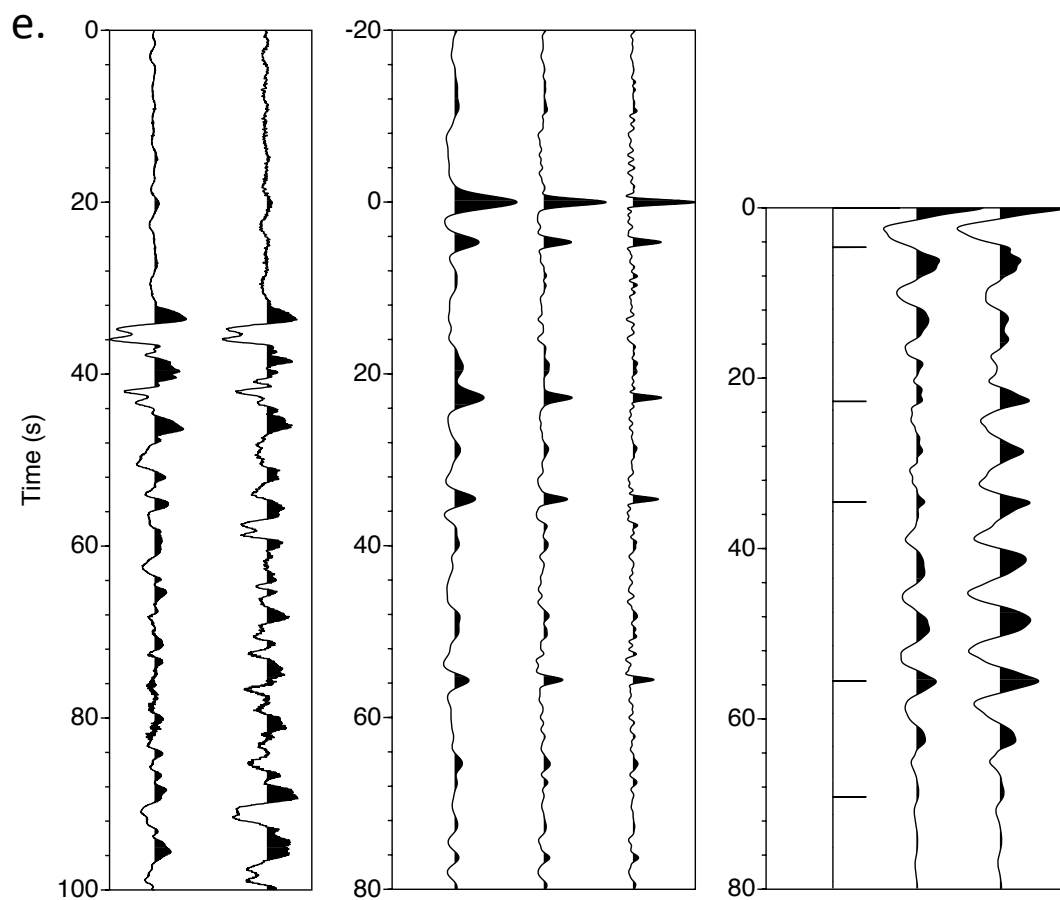


Figure S6

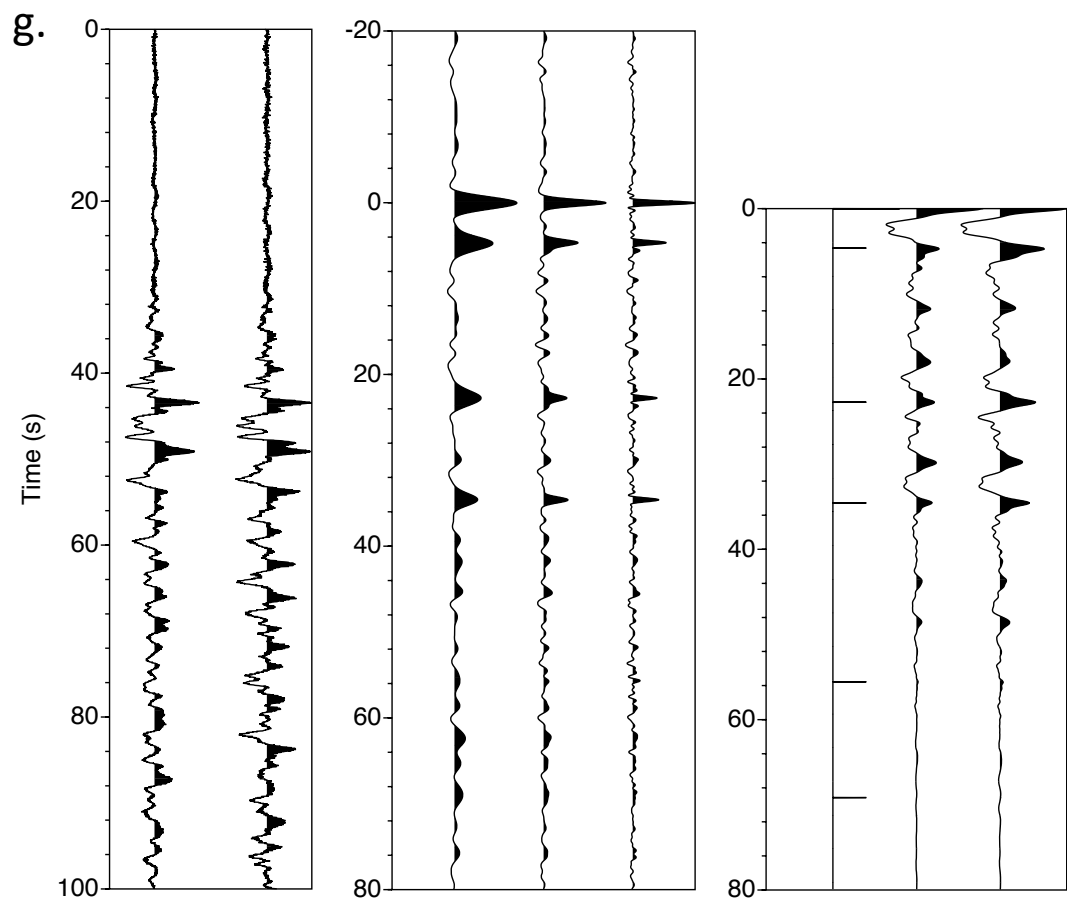


Figure S6

Figure S6. Comparison of deconvolution, autocorrelation, and cross correlation for long-duration effective source wavelets. Results are shown for seven representative earthquakes (events 4, 3, 1, 2, 9, 7, and 5) (Table S1). Effective source wavelets (left panel, first trace) were derived by stacking waveforms for broadband stations deployed north of the Atlantic Coastal Plain (Figure 1). Synthetic seismograms (second trace) then were generated by convolving the effective source wavelets with a series of 6 impulses representing the direct PKIKP (PKPdf) arrival and a pseudo-random time distribution of five reflections, then adding low-level ($S/N \sim 10$) random noise. The middle panel shows the synthetic seismograms deconvolved in the frequency domain by the effective source wavelet using a water-level of 0.001 and a range of Gaussian smoothing parameters ($\alpha = 1, 2, 4$). The beginning and end of traces were linearly tapered over a window of 3 s prior to Fourier transformation. The righthand panel shows the 6 impulses (first trace) used to generate the synthetic seismograms, the zero and positive lags of the autocorrelation (second trace) of the synthetic seismogram, and the zero and positive lags of the cross correlation (third trace) of the synthetic seismogram with the effective source wavelet.

a. Results for event 4 ($M_w = 6.9$; source depth: 208 km; predicted differential time between pPKPdf and PKPdf: ~ 54 s). Deconvolution recovers the amplitudes of all 5 reflections, with minimal spurious energy over other portions of the seismograms. Autocorrelation also recovers the 5 reflections but not with their full amplitude, and also generates appreciable sidelobes. Cross correlation is better than autocorrelation in recovering amplitudes but sidelobes remain.

b. Results for event 3 ($M_w=6.6$; source depth: 62 km; predicted differential time between pPKPdf and PKPdf: ~ 18 s). Deconvolution again recovers the amplitudes of all 5 reflections, but an artifact is generated at the end the trace, where the source-side reflection pPKPdf for the latest event extends past the listening window. Reflections are barely above the level of sidelobes in the autocorrelation, but reflection amplitudes are better recovered by cross correlation. The decrease in the number of samples contributing to the correlations at greater lags suppresses the noise pulse at the end of the trace.

c. Results for event 1 ($M_w=7.3$; source depth: 386 km; predicted differential time between pPKPdf and PKPdf: ~ 134 s). Although source-side scattering for this event begins well after the end of the listening window, the large magnitude generates an effective source wavelet with a duration greater than 20 s, with much of the energy delayed until the middle of the waveform. As a result, the latest reflection at roughly 70 s is just barely recovered and is accompanied in the deconvolved output by artifacts. As with event 3 (Figure S6b), these artifacts do not appear in the correlated traces.

d. Results for event 2 ($M_w=7.1$; source depth: 61 km; predicted differential time between pPKPdf and PKPdf: ~ 17 s). The results are similar to those for event 1 (Figure S6c), but in general are noisier.

e. Results for event 9 ($M_w=6.7$; source depth: 18 km; predicted differential time between pPKPdf and PKPdf: ~ 6 s). For this event and event 5 (Figure S6g), the input trace started

roughly 30 s before the onset of PKPdf, rather than 20 s as used for other events, resulting in a shorter listening window (70 s rather than 80 s). The latest reflection is no longer recovered. For the deconvolved traces, the noise level is similar to that for event 2 (Figure S6d). Correlated traces have a much narrower bandwidth that is dominated by lower frequencies in the effective source wavelet. As a result, the earliest reflection is not recovered in those traces.

f. Results for event 7 ($M_w=7.1$; source depth: 129 km; predicted differential time between pPKPdf and PKPdf: 34 s). Results are similar to those for event 9 (Figure S6e), but because most of the energy is concentrated over later portions of the effective source wavelet, the amplitude of the fourth reflection is not as well recovered in the deconvolved traces. Compared with event 9, the greater bandwidth of the source wavelet results in broader band reflections in the correlated traces.

g. Results for event 5 ($M_w=6.6$; source depth: 20km; predicted differential time between pPKPdf and PKPdf: 7 s). As with event 9 (Figure S6e), the input trace for this event started roughly 30 s before the onset of PKPdf. Coupled with the emergent nature of the source waveform, this results in barely detectable signal levels for the two latest reflections.

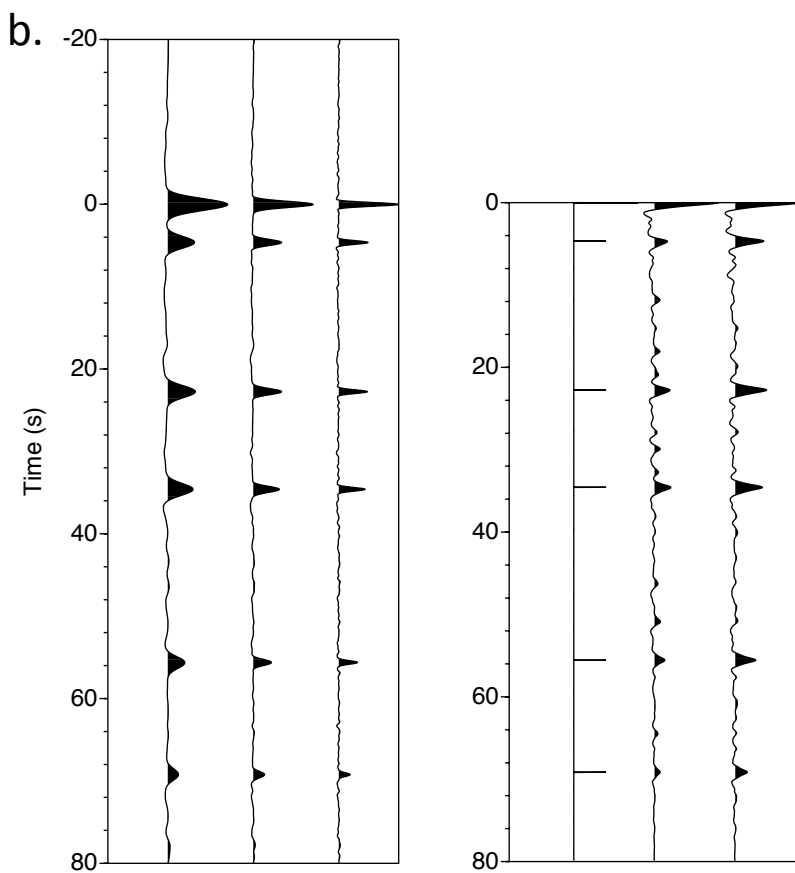
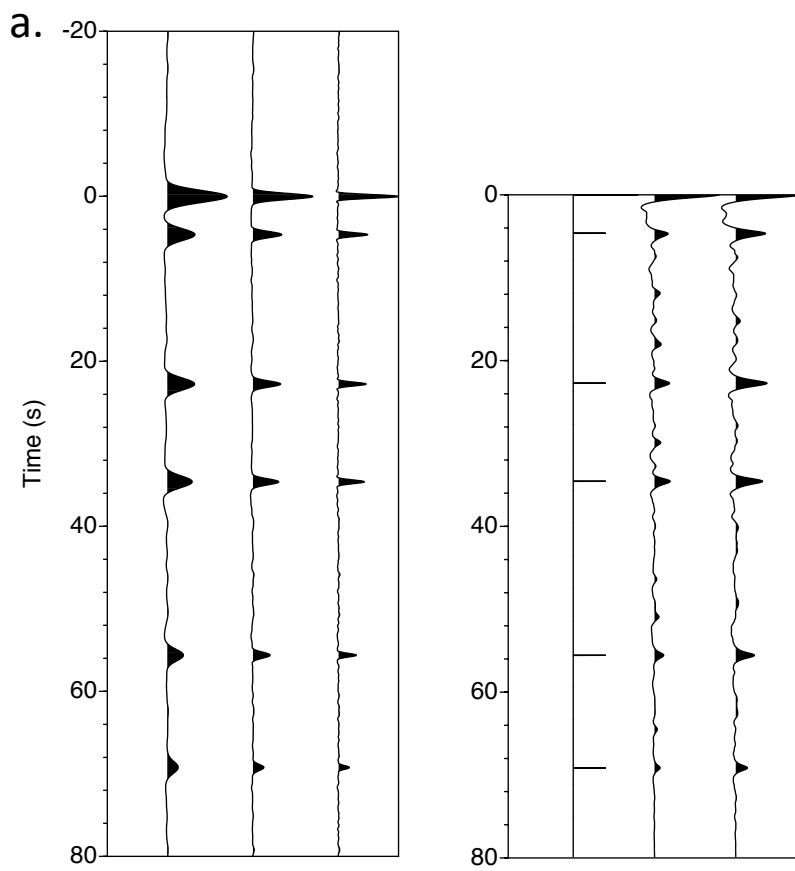


Figure S7

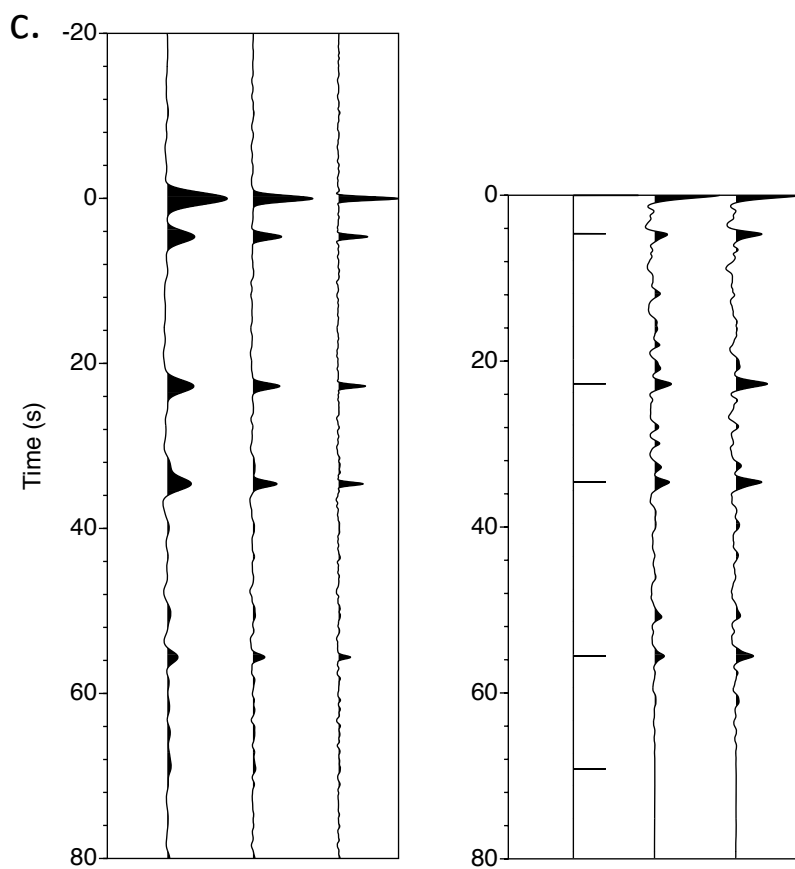


Figure S7

Figure S7. Stacking of filtered traces for multiple earthquakes. Synthetic traces were generated for all the events listed in Table S1, beginning with the effective source wavelets derived by stacking waveforms for stations deployed north of the Atlantic Coastal Plain, then proceeding as described for Figure S6. Left panel: stack of deconvolved traces for a range of Gaussian smoothing parameters ($\alpha=1, 2, 4$). Right panel, first trace: the 6 impulses used to generate the synthetic seismograms; second trace: stack of the zero and positive lags of the autocorrelations of the synthetic seismograms; and third trace: stack of the zero and positive lags of the cross correlations of the synthetic seismograms with the effective source wavelets. Stacking suppresses artifacts in the deconvolved traces but some of the sidelobe energy in the correlated traces remains.

a. Stacks of waveforms for the 16 earthquakes used to generate the output sections shown in Figures 2, 4, S2, and S5 (events 1-16 in Table S1). All reflections are recovered but the two latest reflections are attenuated.

b. Stacks of waveforms for the 8 earthquakes used to generate the output section shown in Figure S3 (events 1-3; 8, 10, 11, 13, 14 in Table S1). Again, all reflections are recovered but the two latest reflections are attenuated.

c. Stacks of waveforms for the 6 earthquakes used to generate the output sections shown in Figures 3 and S4 (events 1, 2, 8, 10, 11, 14 in Table S1). The latest reflection is not recovered because of the shorter listening window (70 s) used for these earthquakes rather than 80 s as used for most of the earthquakes in Figures S7a and S7b).

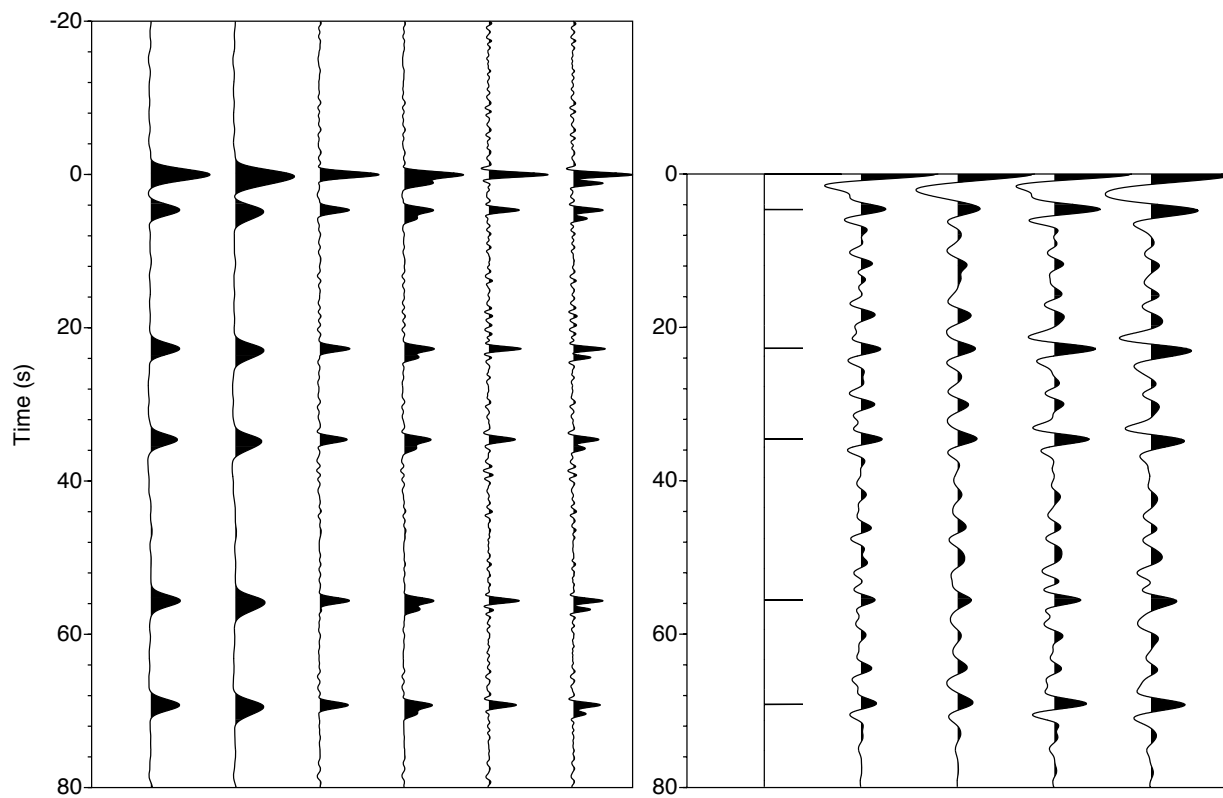


Figure S8.

Figure S8. Comparison of deconvolution, autocorrelation, and cross-correlation for long-duration effective source wavelets. Similar to Figure S6, except for the addition of a second input seismogram (second trace for each pair of traces) generated using a source wavelet that is now the sum of the original source wavelet for event 13 (Table S1) and the same wavelet delayed by 1.1 s, to simulate the effect of differential moveout for PKPdf and PKiKP between stations north of the Coastal Plain and the southernmost station in Line E. The amplitude of the PKiKP contribution is assumed to be half that of the PKPdf contribution, and for simplicity, the phase angle is assumed to be the same.

The left panel shows the synthetic seismograms deconvolved in the frequency domain by the original source wavelet using a water-level of 0.001 and a range of Gaussian smoothing parameters ($\alpha = 1, 2, 4$). The beginning and end of traces were linearly tapered over a window of 3 s prior to Fourier transformation. Each pair of traces shows reflections for coincident PKPdf/PKiKP arrivals (first trace of each pair) and the two arrivals separated by 1.1 s (second trace of each pair), for a given value of α . As expected, differential moveout generates additional cycles for each reflection.

The righthand panel shows the 6 impulses (first trace) used to generate the synthetic seismograms, the zero and positive lags of the autocorrelation of the synthetic seismogram for coincident PKPdf and PKiKP (second trace), the autocorrelation for PKPdf and PKiKP separated by 1.1 s (third trace), and zero and positive lags of the cross correlation of the synthetic seismograms with the original source wavelet, again for coincident PKPdf and PKiKP (fourth trace) and the two arrivals separated by 1.1 s (fifth trace). Differential moveout generates a slight broadening of the waveform, accompanied by a small delay for the cross-correlated waveforms.

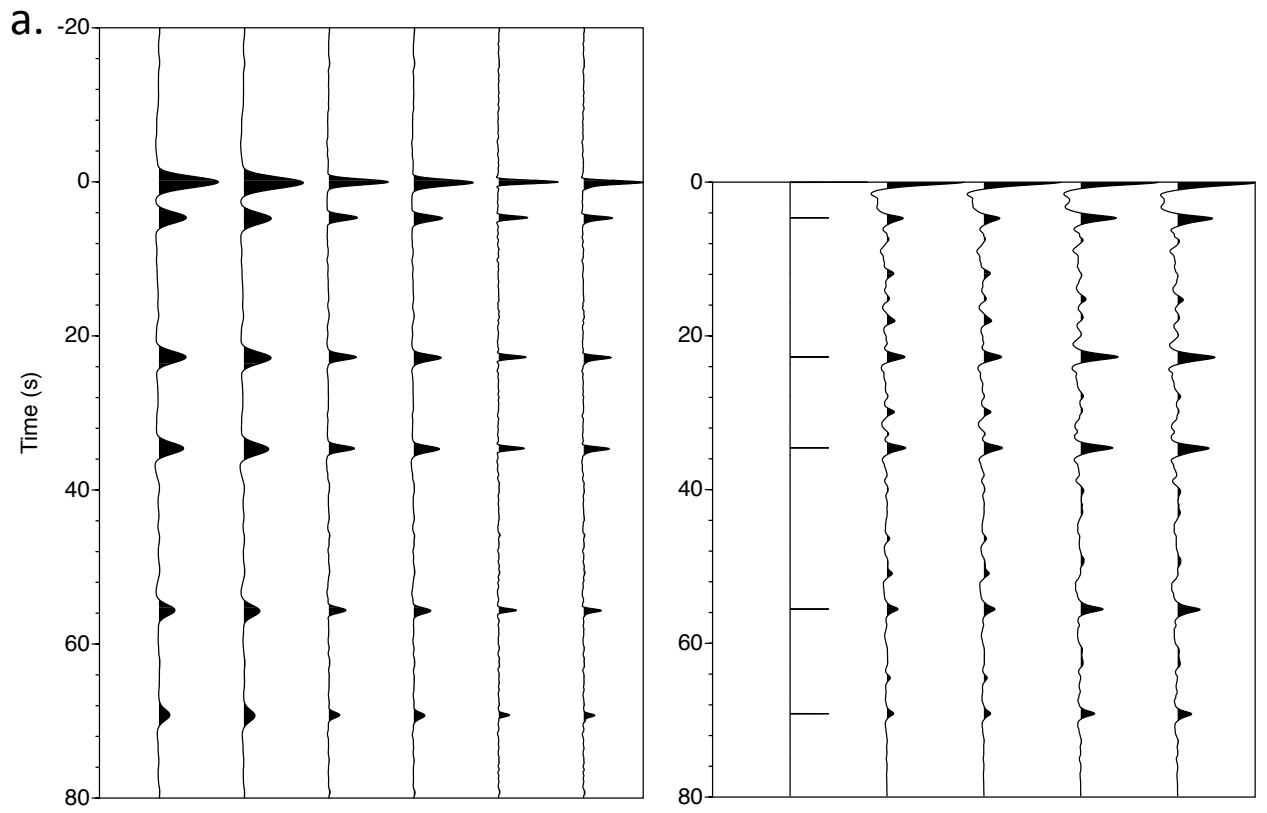


Figure S9

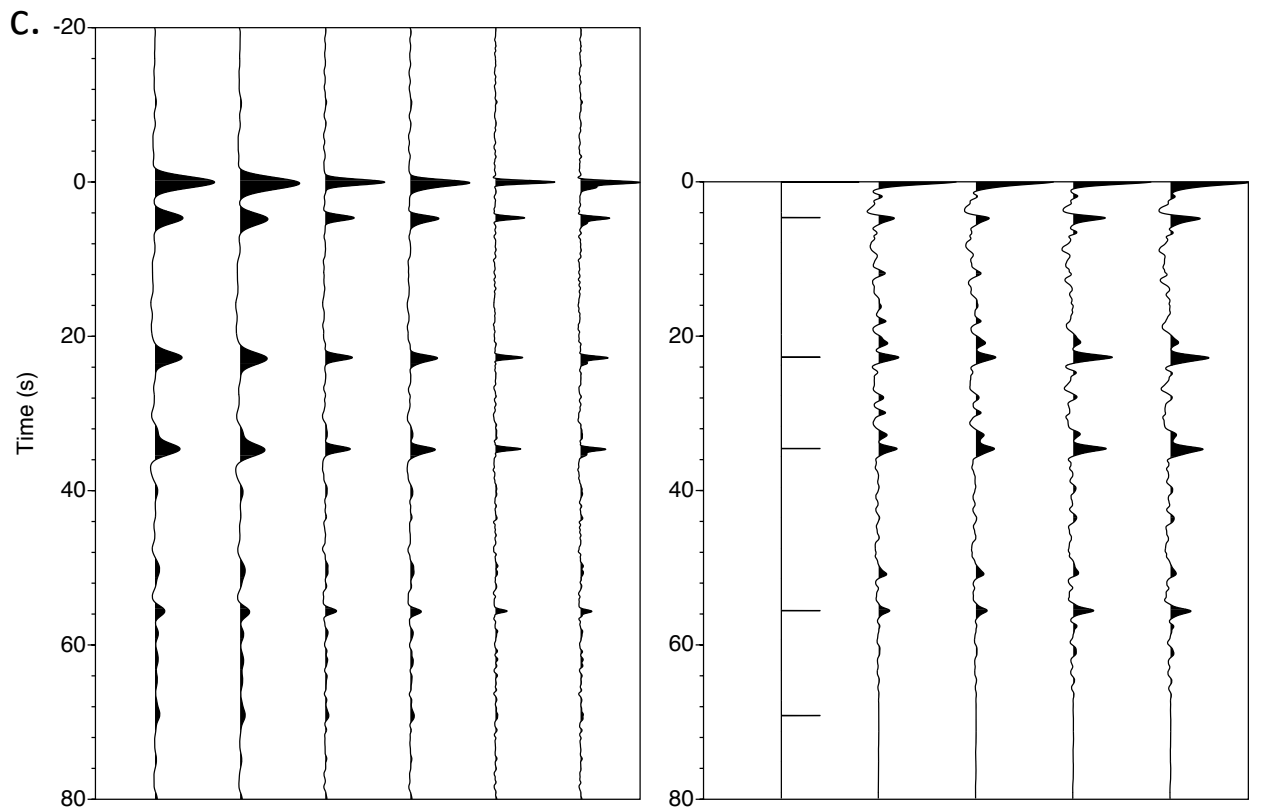
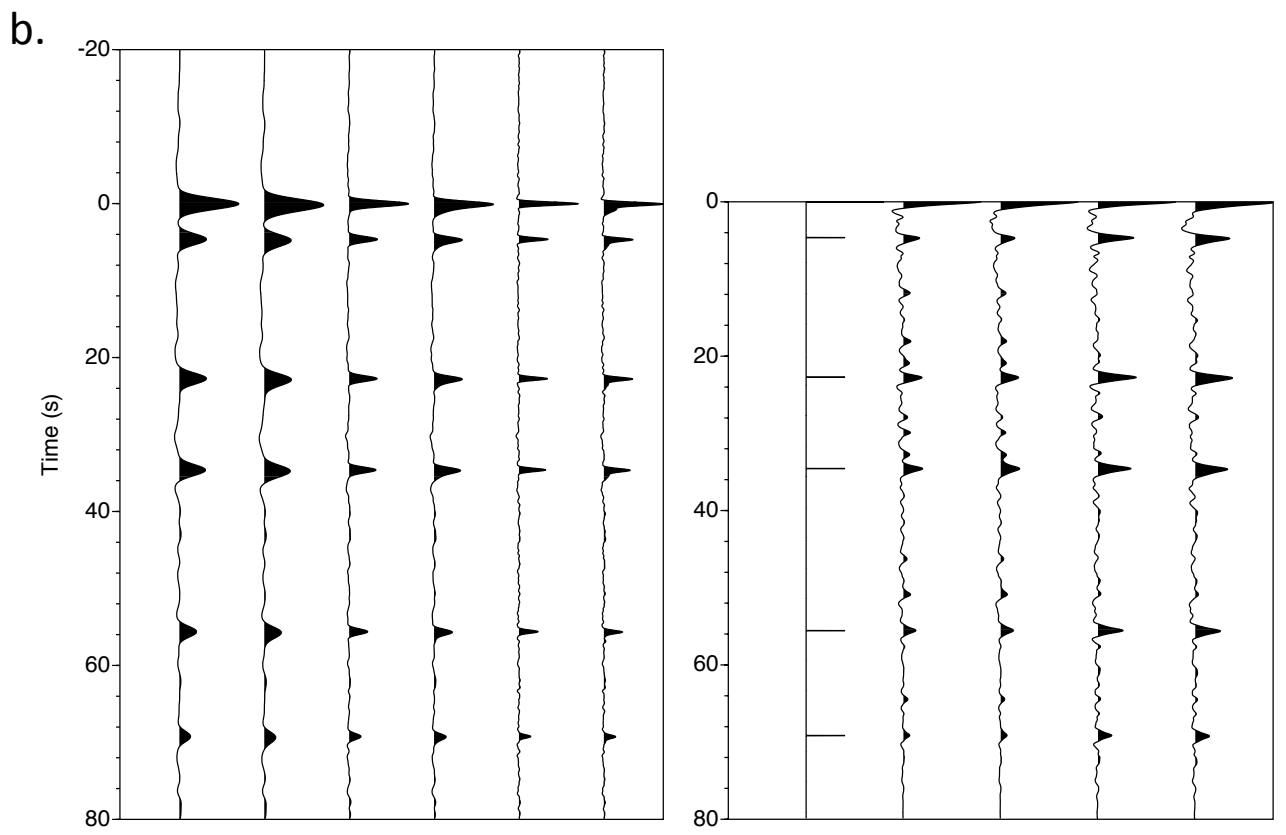


Figure S9

Figure S9. Similar to Figure S8, except that filtered traces have been stacked for multiple earthquakes. Deconvolution and cross correlation were carried out using the source wavelet derived for each event (Table S1).

The lefthand panel shows stacks of synthetic seismograms deconvolved in the frequency domain by the original source wavelet for each earthquake, using a water-level of 0.001 and a range of Gaussian smoothing parameters ($\alpha = 1, 2, 4$). Each pair of traces shows reflections for coincident PKPdf/PKiKP arrivals (first trace of each pair) and the two arrivals separated by 1.1 s (second trace of each pair), for a given value of α .

The righthand panel shows the 6 impulses (first trace) used to generate the synthetic seismograms, stacks of the zero and positive lags of the autocorrelations of the synthetic seismograms for coincident PKPdf and PKiKP (second trace), stacks of the autocorrelations for PKPdf and PKiKP separated by 1.1 s (third trace), and stacks of the zero and positive lags of the cross correlations of the synthetic seismograms with the original source wavelets, again for coincident PKPdf and PKiKP (fourth trace) and the two arrivals separated by 1.1 s (fifth trace).

a. Stacks of waveforms for the 16 earthquakes used to generate the output sections shown in Figures 2, 4, S2, and S5 (events 1-16 in Table S1). Stacking compresses wavelets broadened by differential moveout.

b. Stacks of waveforms for 7 of the 8 earthquakes used to generate the output section shown in Figure S3 (events 1-3; 8, 10, 11, 13 in Table S1; event 14 was not recorded at the southernmost station). In the stack of the deconvolved traces (left panel), wavelets are compressed but some of the wavelet asymmetry remains. In the stack of the cross correlated traces (right panel), wavelets still show a small delay.

c. Stacks of waveforms for 5 of the 6 earthquakes used to generate the output sections shown in Figures 3 and S4 (events 1, 2, 8, 10, 11, in Table S1; again, event 14 was not recorded at the southernmost station). As in Figure S9b, some of the wavelet asymmetry and delay remains.

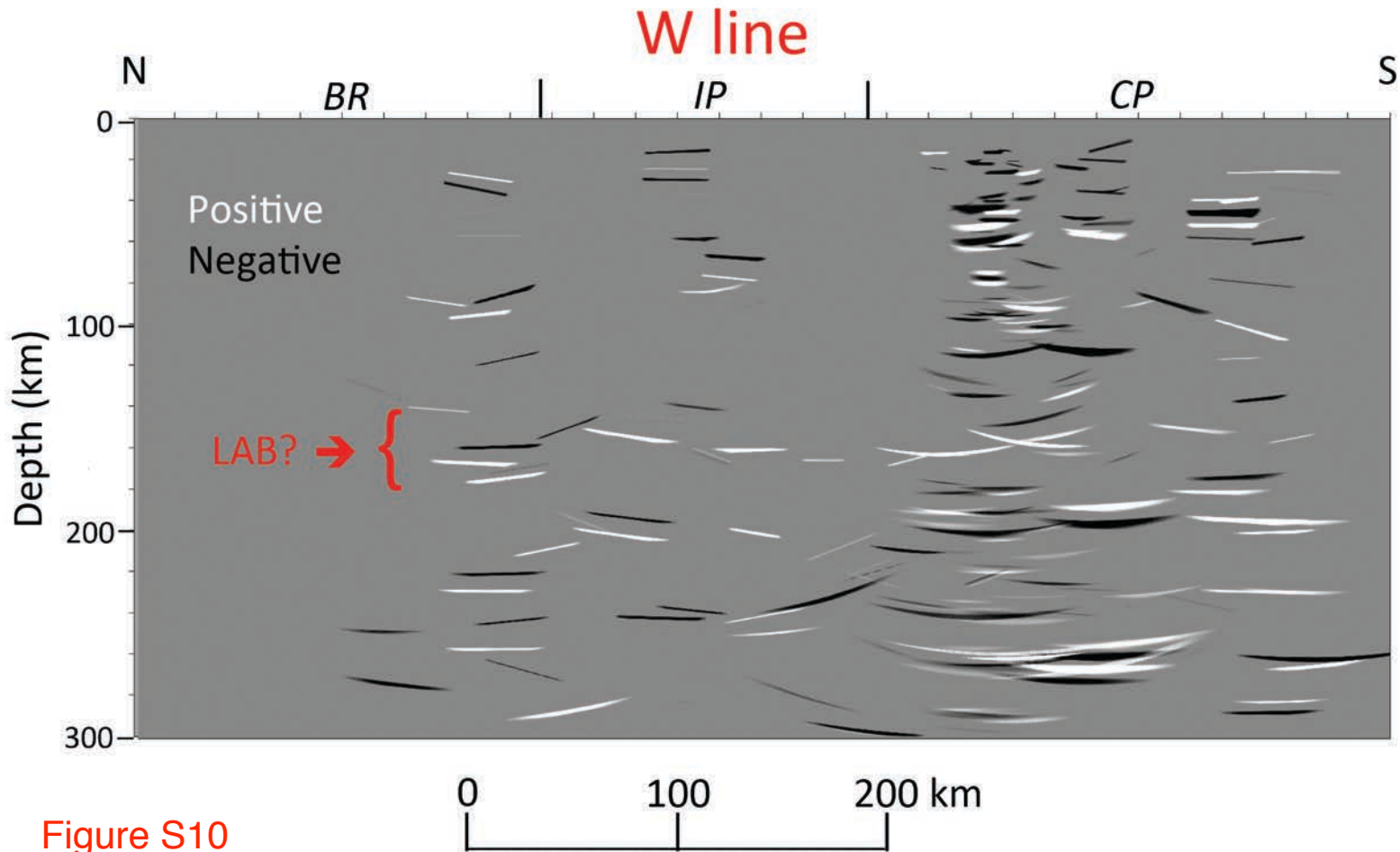


Figure S10

Figure S10. Preliminary migrated section for Line W, showing reflections identified in coherency-filtered slant stacks of small-aperture gathers extracted for events 1, 2, 3, 4, 7, 11, 13, and 16 (Table S1). White: reflections from positive impedance contrasts; black: reflections from negative impedance contrasts.

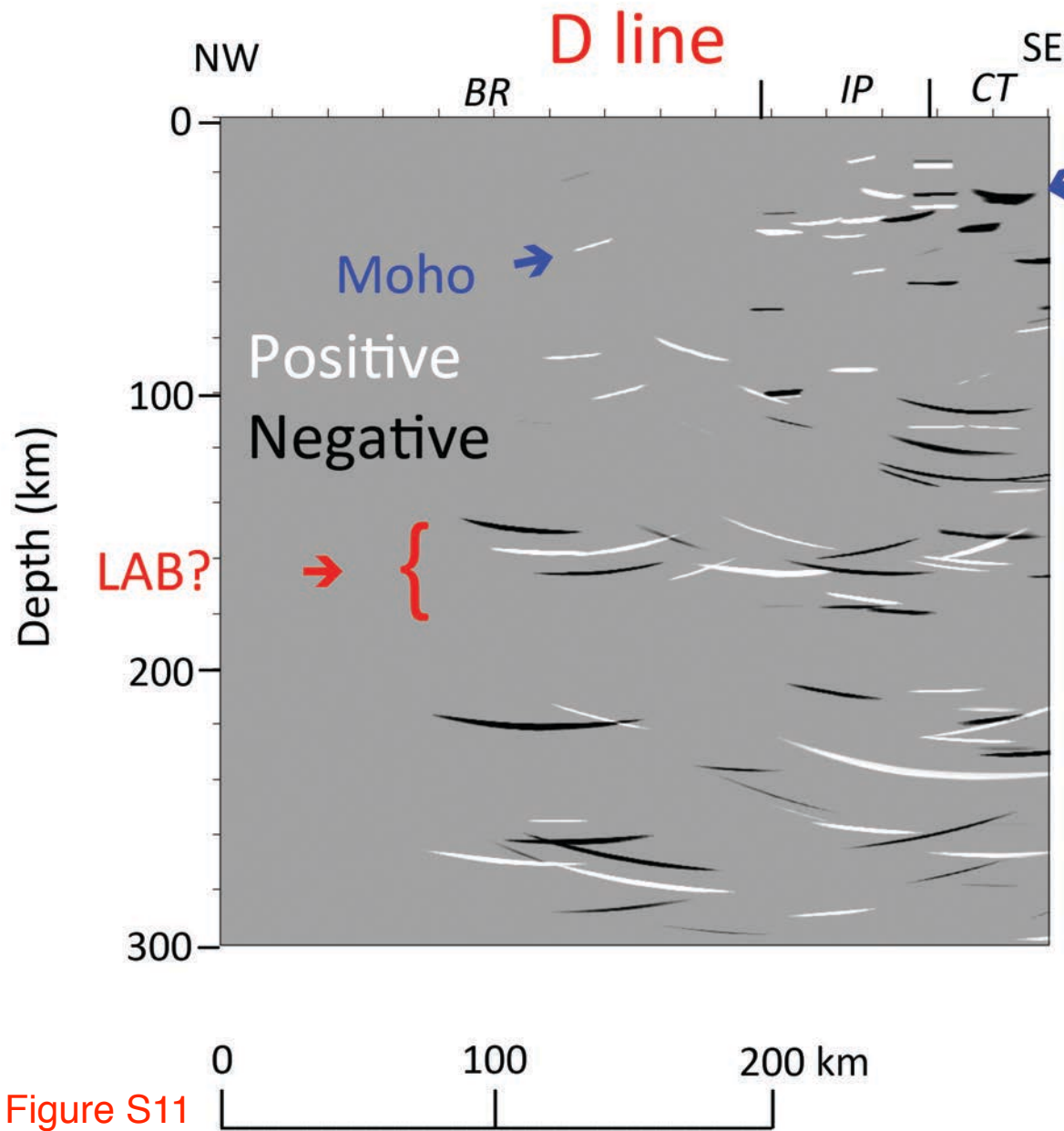


Figure S11

Figure S11. Preliminary migrated section for Line D, showing reflections identified in coherency-filtered slant stacks of small-aperture gathers extracted for events 1, 3, 4, 7, 11, 13, and 16 (Table S1). White: reflections from positive impedance contrasts; black: reflections from negative impedance contrasts.

Table S1. Earthquakes used for analysis of PKIKP phases ^{1,2,3}.

Event #	Date & Time (UT)	Lat. (°N)	Long (°E)	Depth (km)	Magnitude (Mw)	Back-Azimuth (°)	Distance (°)
1	2013-07-07 18:35:31.38	-3.92	153.92	386.3	7.3	D: 286.2-286.7 W: 286.3-283.8 E: 286.5-284.4	117.8-120.0 118.3-119.6 120.4-121.4
2	2014-04-11 07:07:22.81	-6.59	155.05	60.5	7.1	D: 283.0-283.4 W: 283.1-280.5 E: 283.1-281.2	118.5-120.6 119.0-120.0 121.0-121.8
3	2013-07-07 20:30:07.38	-6.02	149.72	62.0	6.6	D: 287.3-287.8 W: 287.4-284.4 E: 287.4-284.9	122.4-124.6 122.9-124.2 125.0-126.1
4	2012-04-17 07:13:49.88	-5.53	147.13	208.2	6.9	D: 289.9-290.1 W: 289.8-286.6	125.3-126.4 124.6-126.1
5	2011-07-31 23:38:58.09	-3.51	144.97	19.6	6.6	D: 293.5-293.8 W: 293.3-290.2	125.5-126.8 125.0-126.8
6	2012-03-21 22:15:05.59	-6.22	146.0	117.7	6.6	D: 290.1-290.3 W: 290.0-286.6	126.4-127.7 125.9-127.4
7	2011-12-14 05:04:57.81	-7.53	146.81	128.5	7.1	D: 288.2-288.4 W: 288.1-284.7	126.6-127.8 126.1-127.5
8	2012-08-31 12:47:35.54	10.81	126.83	44.4	7.6	D: 321.3-322.7 W: 321.6-319.3 E: 322.6-320.7	125.3-127.9 125.9-129.6 128.4-131.4
9	2012-02-06 03:49:13.92	9.92	123.22	17.5	6.7	D: 325.3-326.2 W: 324.9-322.6	129.0-130.4 128.5-132.3
10	2013-10-15 00:12:33.25	9.83	124.12	23.2	7.1	D: 323.6-325.1 W: 323.9-321.5 E: 325.0-323.0	127.5-130.0 128.1-131.9 130.6-133.7
11	2013-04-06 04:42:36.19	-3.51	138.48	66.0	7.0	D: 298.7-299.3 W: 298.8-295.5 E: 299.0-295.1	129.2-131.6 129.8-131.8 132.1-133.8
12	2012-04-21 01:16:53.67	-1.69	134.32	24.4	6.7	D: 304.6-305.0 W: 304.4-300.7	131.9-133.3 131.4-134.0
13	2012-10-17 04:42:31.06	4.18	124.56	338.4	6.0	D: 319.3-320.7 W: 319.6-316.5 E: 320.5-318.0	132.1-134.7 132.7-136.3 135.2-138.1
14	2012-08-26 15:05:37.16	2.19	126.84	91.1	6.6	D: 315.3-316.5 W: 315.5-312.5 E: 316.3-314.6	132.5-135.0 133.1-136.2 135.6-137.2
15	2011-06-13 14:31:23.40	2.54	126.46	66.0	6.4	D: 316.6-317.2 W: 316.2-312.9	133.6-135.0 133.0-136.4
16	2011-12-13 07:52:12.03	0.05	123.06	167.4	6.1	D: 318.6-319.4 W: 318.3-314.6	137.5-138.9 137.0-140.5

¹All 16 events were used for the stacks in Figures 2, 4, S2, and S5

² Events 1, 2, 3, 8, 10, 11, 13, 14 were used for the stacks in Figure S3

³ Events 1, 2, 8, 10, 11, 14 were used for the stacks in Figures 3 and S4

Table S1.

Title: "Table S1. Earthquakes used for analysis of PKIKP phases"

Contents: This table summarizes parameters for the 16 earthquakes used for the paper.

Column 1: Event numbering roughly in order of increasing epicentral distance.

Column 2: "Date": date of the earthquake listed as year-month-day; "Time": Universal time of the earthquake.

Column 3: "Lat. (°N)": latitude of the epicenter in degrees north of the equator

Column 4: "Long. (°E)": longitude of the epicenter in degrees east of the prime meridian.

Column 5: "Depth (km)": depth of the earthquake focus in kilometers.

Column 6: "Magnitude (M_w)": moment magnitude of the earthquake.

Column 7: "Back-Azimuth (°)": the range in back-azimuth in degrees clockwise from north from SESAME stations to the epicenter. "E", "W", and "D" refer to back-azimuths for stations along the N-S striking Eastern line, the N-S striking Western line, and the NW-striking line, respectively (Figure 1).

Column 8: "Distance (°)": the range in angular distance between the stations and epicenter.